Carrier Leakage Dynamics in Terahertz Quantum Cascade Lasers

Asaf Albo and Yuri V. Flores

***Abstract*— We analyze the output power versus temperature characteristics of two GaAs/$Al_{0.15}Ga_{0.85}$As terahertz quantum cascade lasers (THz-QCLs) with maximum operating temperature T_{max} = 200 and 177 K as well as of one GaAs/$Al_{0.30}Ga_{0.70}$As THz-QCL with T_{max} = 150 K and identify the thermally-activated leakage paths responsible for the laser performance degradation as the temperature increases. We identify the specific carrier leakage path active in each THz-QCL structure and are able to reconstruct the output power versus temperature profile over the entire laser operation range. We find that using high barriers in the active region design virtually eliminates carrier leakage from the upper laser level into the continuum, opening a non-radiative scattering path from the upper into the lower laser level parallel to standard electron-LO-phonon emission. This effect, together with the reduced leakage from the lower laser level into the continuum in the high-barrier device, significantly contributes to the T_{max} decrease from 177 to 150 K. We further show how electron leakage from the lower laser level into the continuum is enhanced in a GaAs/$Al_{0.15}Ga_{0.85}$As design with thin barriers, significantly improving the laser performance (T_{max} = 200 K). Finally, we propose future design strategies for highly temperature-insensitive THz-QCLs. Our approach offers a straightforward method to analyze and troubleshoot thermally-activated carrier leakage dynamics in THz-QCLs.**

***Index Terms*— Intersubband transitions, quantum cascade laser, terahertz emission.**

I. Introduction

TERAHERTZ quantum cascade lasers (THz-QCLs) [1] are unique light sources in the submillimeter wavelength region of the electromagnetic spectrum. To date, THz-QCLs are exploited in a reduced number of applications, most outstandingly in heterodyne spectroscopy for infrared astronomy [2]–[4]. The spectrum of potential applications of THz-QCLs is however diverse, including fast and sensitive detection of hidden explosives and illicit drugs, biomedical imaging and ultrafast on-chip gas spectroscopy.

Moreover, further diversification of THz-QCL-based technology strongly depends on the improvement of key laser performance quantities as for example the maximum operating temperature T_{max}. Laser performance characteristics of THz-QCLs continuously improved since the first demonstration of a THz-QCL in 2002 [1]. Unfortunately, this trend has decelerated in the last years and reported T_{max} values converged to $\sim$ 200 K [5], [6]. Besides technological factors, the slow progress on T_{max} is related to the complexity of QCL active region design as well as to an incomplete understanding of the temperature-driven electron transport in THz-QCLs. In this context, thermally activated leakage of electrons out of THz-QCL active region states deserves particular attention.

As a matter of fact, thermally activated electron leakage has been always referred in THz-QCL literature as a potential discrepancy source between expected temperature-dependent laser characteristics and the poorer de facto laser performance. However, only few works have explicitly addressed this topic, offering only partial understanding of the mechanisms that govern thermally activated leakage in THz-QCLs. The main difficulty in the analysis of thermally activated electron leakage in QCLs is the fact that no direct measurement of it can be done. In the case of mid-infrared QCLs, where electron transport is fairly described without consideration of resonant tunneling characteristics, indirect ways to measure the thermally activated leakage current are available [7]–[13]. On the other hand, in THz-QCLs, the analysis of the impact of thermally activated electron leakage on measured laser performance indicators (e.g. light output power) is offered as an alternative [14]–[17].

In essence [17], the measured output power versus temperature of any THz-QCL structure can be described by considering the effect of three thermally activated electron leakage mechanisms on the population inversion, and, consequently, on the laser gain:

1) thermally activated electron scattering from the upper into the lower laser level by longitudinal-optical (LO) phonon emission
2) thermally activated leakage of electrons from the upper laser level into the continuum or into excited bound states
3) thermally activated leakage of electron from the lower laser level into the continuum or into excited bound states

As shown in [14], process 1 is maximized in devices with vertical radiative transition due to the increased spatial overlap between upper and lower laser wavefunctions. Furthermore, as explained in [15] and [16], switching to diagonal radiative transitions promotes thermally activated leakage from the

Manuscript received March 29, 2017; revised June 30, 2017; accepted August 1, 2017. Date of publication August 15, 2017; date of current version August 31, 2017. The work of A. Albo was suppoerted by the Bar-Ilan University Engineering Faculty Fellowship. The work of Y. V. Flores was supported by the Research Fellowship Program of the German Research Foundation, DFG, under Grant FL945/1-1. *(Corresponding author: Asaf Albo.)*

A. Albo is with the Faculty of Engineering, Bar-Ilan University, Ramat Gan 5290002, Israel (e-mail: asafalbo@gmail.com).

Y. V. Flores is with the Research Laboratory of Electronics, Massachusetts Institute of Technology, Cambridge, MA 02139 USA (e-mail: yvf@mit.edu).

Color versions of one or more of the figures in this paper are available online at http://ieeexplore.ieee.org.

Digital Object Identifier 10.1109/JQE.2017.2740261

0018-9197 © 2017 IEEE. Personal use is permitted, but republication/redistribution requires IEEE permission.
See http://www.ieee.org/publications_standards/publications/rights/index.html for more information.

upper laser level into the continuum or into excited bound states (process 2). More recently, we showed in [17] that process 3 is also present in THz-QCLs and that it can be fast enough to effectively counteract the population inversion decrease that arises from processes 1 and 2 as the temperature increases. In essence, inclusion of these three temperature sensitive mechanisms provides a fair description of the impact of thermally activated leakage on the performance of state of the art THz-QCLs. However, some ambiguity exists in the choice of the excited state responsible for triggering the escape of electrons from the upper (or lower) laser level and one may tend to assume that this state is confined in the same quantum well than the upper (or lower) laser state.

In this work we show that the correct identification of the excited state that triggers thermally activated leakage is crucial for a confident analysis of the carrier dynamics in THz-QCLs based on the interpretation of output power vs. temperature experimental data. The current work should be considered as an extension of our previously published approach [17] in order to account for temperature and subband-dependent electron temperatures and also active region design-dependent leakage paths. The latter point becomes particularly relevant for a confident interpretation of experimental data for QCL active region designs that use different potential barrier heights, as we explain further down in section IV.

We find that the specific excited state that triggers the escape of electrons into the continuum is not necessarily the next state with higher energy than the upper laser level nor it is necessarily confined in the same quantum well. Furthermore, by identifying the correct excited state in individual GaAs/$Al_xGa_{1-x}As$ THz-QCL designs we are able to fit the output power vs. temperature experimental data over the entire laser operation range. We find that using $Al_{0.30}Ga_{0.70}As$ barriers in the active region design eliminates carrier leakage from the upper laser level into the continuum yet it opens a non-radiative scattering path from the upper into the lower laser level parallel to standard electron-LO-phonon emission. This effect, together with the reduced leakage from the lower laser level into the continuum, significantly contributes to the T_{max} decrease from 177 K to 150 K in an analyzed GaAs/$Al_{0.30}Ga_{0.70}As$ device. We further show how electron leakage from the lower laser level into the continuum is enhanced in a GaAs/$Al_{0.15}Ga_{0.85}As$ design with thin barriers, significantly improving the laser performance (T_{max} = 200 K). Finally, we propose design strategies for future highly temperature-insensitive THz-QCLs.

II. Investigated Lasers

We choose to investigate three state of the art GaAs/$Al_xGa_{1-x}As$ THz-QCLs: two devices with low (x = 0.15) barriers and resonant phonon design with diagonal optical transition (device V775 in [5] and device VB0605 in [15]), referred in the following as devices LB1 and LB2, respectively, and one high ($x = 0.30$) barrier design (device VB0676 in [16]), referred in the following as device HB. Design parameters and laser performance details are summarized in Tab. I. The investigated designs differ in the design parameters, doping and processing steps. The

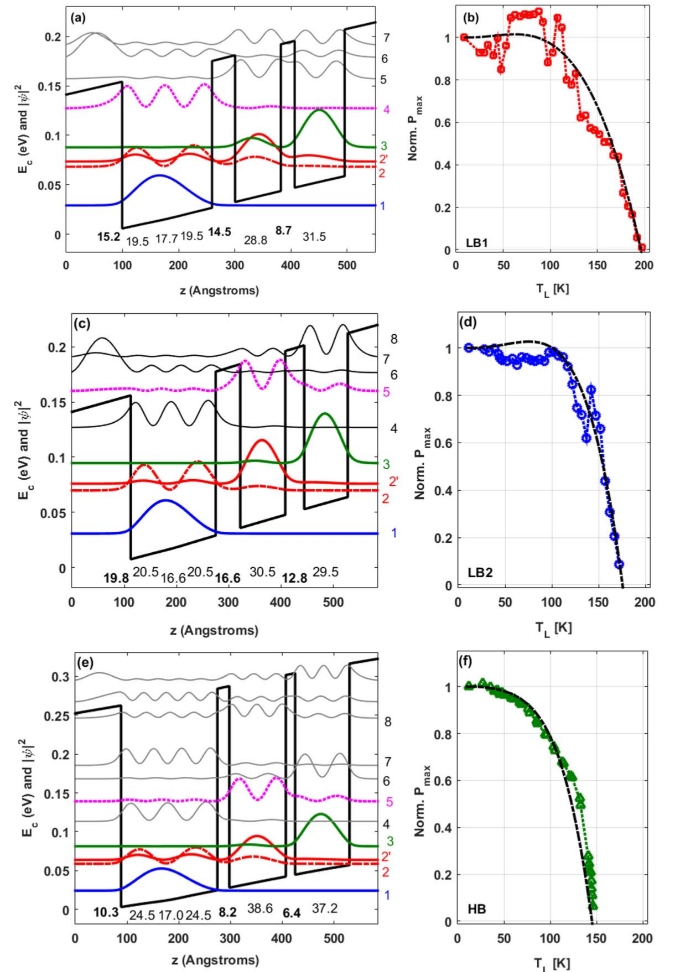

Fig. 1. Conduction band profile at design bias (left) and measured normalized light output power versus temperature (right, symbols) for the devices investigated in this work: LB1 (a) and (b), LB2 (c) and (d), and HB (e) and (f), respectively. Layers thicknesses (in monolayers) are indicated. Relevant wavefunctions are colored and labeled. The dashed-dotted black lines represent calculated values as explained in the text. Additional design parameters and measurement details for devices LB1, LB2 and HB can be found in the original publications [5], [15], and [16], respectively.

THz-QCL wafers are processed into metal-metal ridges as reported in the original references, leading to a nearly unity optical confinement factor in the direction perpendicular to the heterostructure planes [18]. Devices LB2 and HB use Au-Au as vertical optical waveguide and device LB1 uses Cu-Cu. Devices LB2 and HB have by a factor of ∼3 lower oscillator strength f and a by a factor of ∼2 larger doping than device LB1. The original idea here was to compensate the reduced gain (lower oscillator strength) by increasing the total number of available mobile carriers (doping level) in the QCL [19]. Device HB was designed to emulate the wavefunctions alignment of device LB2, yet using higher barriers ($Al_{0.30}Ga_{0.70}As$ instead of $Al_{0.15}Ga_{0.85}As$) [16].

Figure 1 shows the reduced conduction band profile of the investigated lasers together with the measured normalized maximum light output power P_{max} vs. temperature. We see that the P_{max} profiles are quite different for this set of devices. In the low barrier devices (LB1 and LB2) we observe

TABLE I
DESIGN PARAMETERS AND PERFORMANCE

Device /Ref.	Ω_{inj} (meV)	Ω_{ext} (meV)	$h\nu$ (meV)	f	J_{th}(10 K) (A/cm^2)	J_{max}(10 K) (A/cm^2)	ΔJ(10 K) (A/cm^2)	T_{max} (K)	Layer sequence / doping level	Process details
LB1 [5]	2.76	5.94	11 − 14	0.58	975	1615	640	200	**15.2**/29.5/**8.7**/28.8/**14.5**/56.6 GaAs/**$Al_{0.15}Ga_{0.85}As$** (228 periods) 6×10^{16} cm^{-3} in the centered 17.7 ML of underlined well	metal-metal (Ta/Cu) wet etched
LB2 [15]	1.56	3.67	16 − 17	0.2	246	825	579	177	**19.8**/29.5/**12.8**/30.5/**16.6**/57.6 GaAs/**$Al_{0.15}Ga_{0.85}As$** (210 periods) 1.24×10^{17} cm^{-3} in the center 17 ML of underlined well	metal-metal (Ta/Au) dry etched
HB [16]	1.77	4.29	16 − 17	0.2	457	851	394	150	**10.3**/37.2/**6.4**/38.6/**8.2**/65.9 GaAs/**$Al_{0.30}Ga_{0.70}As$** (213 periods) 1.24×10^{17} cm^{-3} in the center 17 ML of underlined well	metal-metal (Ti/Au) dry etched

Indicated are, from left to right, the device name and original reference, injection anticrossing energy, extraction anticrossing energy, measured emission frequency range, oscillator strength, threshold current density at 10 K, maximum current density at 10 K, dynamic range at 10 K, maximum operating temperature, layer sequence and (n-type) doping details, and processing details of the metal-metal (used metals indicated in scopes) waveguide Fabry-Pérot ridges. These laser performance parameters are measured for (∼2 mm × 150 μm) ridges in pulsed operation mode at a low (0.02 %) duty cycle. The active region thicknesses are in all cases ∼10 μm.

nearly constant values of P_{max} up to ∼120 K followed by a continuous decay as the temperature increases (Fig. 1b, 1d). As explained in [17], this kind of temperature stabilization up to a certain temperature value is a consequence of thermally activated carrier leakage of electrons leaving the lower laser level through excited states. The electron flow rate associated to this transport mechanism can be fast enough to effectively counteract the population inversion decrease that arises from the remaining non-radiative scattering processes, contributing positively to laser gain. Furthermore, this effect (nearly constant P_{max} up to a certain temperature value) is virtually absent in device HB (Fig. 1f). As we learn further down in section IV, this is related to the strong reduction of thermally activated leakage of carriers out of the lower laser level that is induced by the high potential barriers.

Figure 1 includes also calculated values for the output power vs. temperature. We calculate these data extending the approach of [17] to account for temperature and subband-dependent electron temperatures and for design-dependent thermally activated leakage paths. In the next section we explain our extensions to the basic model of [17] and in Section IV we apply our analysis approach to the investigated QCL structures.

III. THEORETICAL FRAMEWORK

As in [17], we build our approach on a reduced three levels scheme to represent the QCL active region states. Within this framework, the QCL energy levels of Fig. 1 are projected to an effective energy scheme that includes the upper laser level, the lower laser level and the injector level. (The lower laser level doublet formed by states 2 and 2′ in Fig. 1 is treated as a single effective level [17], referred in the following as state 2.) In essence, this approach idealizes the continuum/excited state as a virtual state wherefrom the carriers are assumed to be immediately recaptured in a non-lasing path back into the injector state of the next downstream cascade. Electrons are able to escape from the upper and lower laser levels into the continuum or into an excited bound state. By considering the impact of these thermally activated escape processes into the lifetimes of the upper and lower laser levels -in addition to standard non-radiative scattering processes (LO-phonon emission from the upper into the lower laser state and LO-phonon emission from the lower laser level)- we estimate the temperature-dependent population inversion and light output power.

For further details on this approach we refer the interested reader to [17]. In the current work we extend this approach in order to account for i) an active region design-dependent excited state that triggers the thermally activated escape of electrons and ii) subband and temperature-dependent electron excess temperatures.

A. Active Region Design-Dependent Thermally Activated Electron Escape Paths

Figure 2 shows reduced three levels schemes to represent electron transport in the investigated QCL structures. Fig. 2a is used for the analysis of the low barrier designs (devices LB1 and LB2) and Fig. 2b is used for the analysis of the high barrier design (device HB).

In the **low barrier devices** (Fig. 2a), a portion of electrons in the upper (level 3) and lower (level 2) laser level scatter into an excited bound state, wherefrom they tunnel through the barriers that separate them from the continuum and are recaptured by the injector state 1 of the next module.

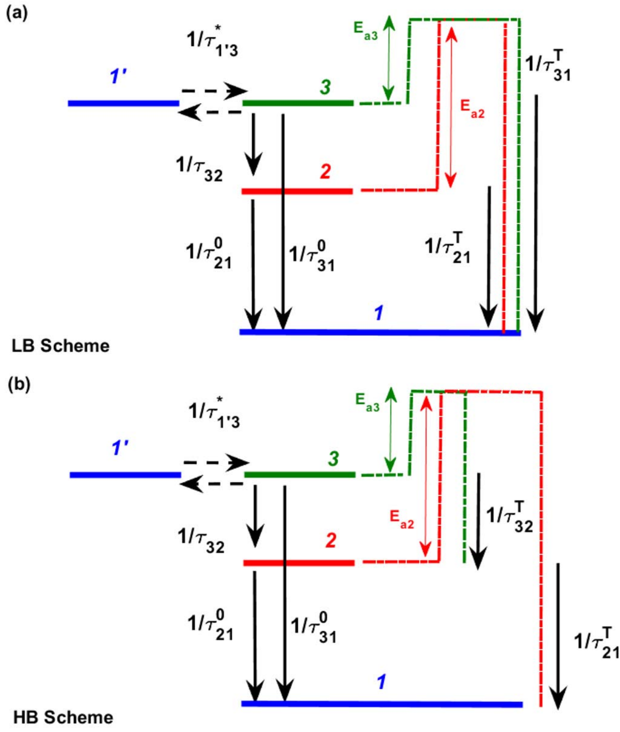

Fig. 2. Reduced 3-level QCL active region scheme with (a) $Al_{0.15}Ga_{0.85}As$ and (b) $Al_{0.30}Ga_{0.70}As$ barriers. Black arrows represent relevant non-radiative scattering paths with corresponding scattering times. Energy levels are colored in analogy to Fig. 1. Dashed black arrows represent resonant tunneling between injector $1'$ and upper laser state 3. State 1 is the injector state of the next cascade. Vertical dashed-dotted lines represent energy barriers or activation energies $E_{a(2,3)}$ for escape into excited states that are strongly coupled with the continuum (upper panel, (a)) or into excited bound states (lower panel, (b). The resonant tunneling time $\tau^*_{1'3}$ goes into calculations of the output power following the method of [14].

As explained in detail in [17], the effect of that leakage path on the lifetimes of levels 3 and 2 is represented by:

$$\textbf{LB}\quad \begin{aligned} &(\tau_{32}^{tot})^{-1} = \tau_{32}^{-1} = (\tau_{32}^{0})^{-1} e^{\frac{E_{32}-E_{LO}}{kT_{e_3}}}, \\ &(\tau_{31}^{tot})^{-1} = (\tau_{31}^{0})^{-1} + (\tau_{31}^{T})^{-1} \\ &(\tau_{21}^{tot})^{-1} = (\tau_{21}^{0})^{-1} + (\tau_{21}^{T})^{-1}, \end{aligned} \tag{1}$$

where τ_{ij}^{tot} is the total non-radiative scattering time from level i into level j, τ_{32}^{-1} is the scattering time from level 3 into level 2 through LO-phonon emission, τ_{ij}^{0} is the raw electron-LO phonon scattering time from level i into level j, E_{LO} is the LO-phonon energy, $E_{ij} = E_i - E_j$ is the intersubband energy spacing between levels i and j, k is the Boltzmann constant, and τ_{ij}^{T} represents the lifetime reduction in state i due to thermally activated escape through an excited bound state and consequent recapture into level j. Lifetimes τ_{ij}^{0} are calculated using a standard Fröhlich interaction calculator and τ_{ij}^{T} are calculated as [17]:

$$\left(\tau_{ij}^{T}\right)^{-1} = \frac{kT_{e_i}}{8\pi\hbar}\frac{N_{AV}^{i}}{N_i}, \tag{2}$$

where, $\hbar$ is the reduced Planck constant, T_{e_i} is the electron temperature of subband i, N_i is the total sheet density of subband i, and N_{AV}^{i} is the portion of electrons from subband i that left this subband through an excited state located at $E_i + E_{a_i}$ and tunneled through the $2-3$ barriers that separate them from the continuum. Following [17], N_{AV}^{i} is calculated as:

$$N_{AV}^{i} \approx (m^*/\pi\hbar^2)(kT_{e_i})T_i \exp\left(-E_{a_i}/kT_{e_i}\right), \tag{3}$$

where m^* is the electron effective mass in the quantum well material, E_{a_i} is the energy barrier (or activation energy), and T_i is the total transmission coefficient associated with the specific excited resonance and barriers that are relevant for the escape process from level i (calculated as in [20, Sect. 7.5]).

In the **high barrier device** (Fig. 2b), we find that the carrier leakage paths differ from the low-barrier cases so that the carrier transport picture goes in this case as follows: Electron escape from level 3 into the continuum is virtually suppressed by the high barriers of device HB. Instead of scattering into the continuum, excited electrons from level 3 tunnel through a single potential barrier (6.4 monolayers thick barrier in Fig. 1e) and then relax into the lower laser level. This leakage path represents a non-radiative scattering channel for electrons that acts in parallel to standard electron-LO-phonon emission from level 3 into 2. Such leakage channel has been described before by Kumar *et al.* in [21] for a low-barrier, two-well $GaAs/Al_{0.15}Ga_{0.85}As$ THz-QCL. Interestingly, we find that this kind of leakage path remains inactive in the low-barrier structures LB1 and LB2 investigated in this work -presumably because of a strong coupling of the excited states and the continuum levels in those designs- so that it emerges only in the high-barrier design HB due to the reduced coupling between the excited bound and continuum states in this device. Similarly, in the high barrier device HB, escape of electrons out of the lower laser level through the excited state is strongly reduced by the high barriers, although not completely suppressed. To summarize, in the high barrier device, the effect of thermally activated leakage on the lifetimes of levels 3 and 2 is represented by:

$$\textbf{HB}\quad \begin{aligned} &(\tau_{32}^{tot})^{-1} = \tau_{32}^{-1} + (\tau_{32}^{T})^{-1} = (\tau_{32}^{0})^{-1} e^{\frac{E_{32}-E_{LO}}{kT_{e_3}}} + (\tau_{32}^{T})^{-1}, \\ &(\tau_{31}^{tot})^{-1} = (\tau_{31}^{0})^{-1} \\ &(\tau_{21}^{tot})^{-1} = (\tau_{21}^{0})^{-1} + (\tau_{21}^{T})^{-1}, \end{aligned} \tag{4}$$

In order to calculate Eq. (1) and (4) one needs to specify which excited state is active in each active region design. As explained in [15], a fit of output power vs. temperature experimental data using Arrhenius-like functions provides an approximation of the activation energy associated to the thermally activated escape of charge carriers. The authors analyzed devices LB2 and HB using that method and found in [16] that an excited resonance located at ~60 meV above the upper laser level was responsible for the output power drop as the temperature increases. A similar analysis on device LB1 shows that an excited resonance located around ~45±10 meV above the upper laser level drives the output power decrease as the temperature increases. Considering those values and comparing them to the calculated energy levels of Fig. 1, we conclude that the excited states triggering thermally activated leakage in the investigated QCL structures are: level 4 in

device LB1 (Fig. 1a), level 5 in device LB2 (Fig. 1c) and level 5 in device HB (Fig. 1e). These levels are highlighted in pink in Fig. 1.

It is important to mention that these schemes are found after fitting experimental data (Fig. 1 and section IV). We point out that several transport schemes have been tested in the course of this investigation and the design schemes presented in Fig. 2 were found to deliver by far the best fits to the data (Fig. 1). The schemes in Fig. 2 are meant to provide a simple and simultaneously effective description of electron transport in the investigated THz-QCLs. Whereas more advanced models [20], [22] can be used for more elaborated description, we consider that our approach catches the essence of the underlying physics.

B. Subband and Temperature-Dependent Electron Excess Temperatures

As explained in the previous section, subband electron temperatures T_{e_i} are to be known in order to compute Eq. (1) – (4). These values go indirectly into calculations via the so-called electron excess temperature $T_{ex_i} = T_{e_i} - T_L$ of the upper ($i = 3$) and lower ($i = 2$) laser state subbands. T_{ex_i} values are always positive as subband electron temperatures are always larger than the lattice temperature, T_L [23], [24].

In [17], temperature-independent yet subband-dependent T_{ex_i} values were taken for the upper ($i = 3$) and lower ($i = 2$) laser level. Nonetheless, during the course of this investigation we learned that a more accurate description of T_{ex_i} is needed in order to understand the electron transport in the investigated devices. In this work we use the more realistic case of subband- and temperature-dependent excess temperatures, i.e. $T_{ex_i} = T_{ex_i}(T_L)$.

In general terms, T_{ex_i} is expected to decay as the lattice temperature increases [14], [25]. At low temperatures there is significant electron heating in all subbands due to the dominance of elastic scattering and, at higher temperatures, LO-phonon scattering becomes dominant and leads to an efficient cooling of electrons towards the lattice temperature. A typical profile of $T_{ex_i}(T_L)$ for different THz-QCL subbands is shown in Fig. 3 (solid dots). These data points are calculated for a resonant phonon THz-QCL [14], [25] and are showed here for illustration purposes. In the present work, we use the functions $T_{ex_3}(T_L) = 100\exp(-T_L/85)$ and $T_{ex_2}(T_L) = 55 + 100\exp(-T_L/85)$ to phenomenologically describe the excess temperatures in the upper and lower laser levels. Resulting values of $T_{ex_{(3,2)}}(T_L)$ are included in Fig. 3.

These functions have been found to lead to very good fits of the experimental output power vs. temperature data, as explained in section IV. It is important to note that we use here equal values of $T_{ex_{(3,2)}}(T_L)$ for all devices. In reality, we expect slightly different $T_{ex_{(3,2)}}(T_L)$ profiles for each particular THz-QCL. We consider that the usage of equal $T_{ex_{(3,2)}}(T_L)$ values for the investigated devices provides our approach further simplicity without falling in physical inaccuracy.

In the next section we illustrate the implications of this electron transport picture on the laser performance.

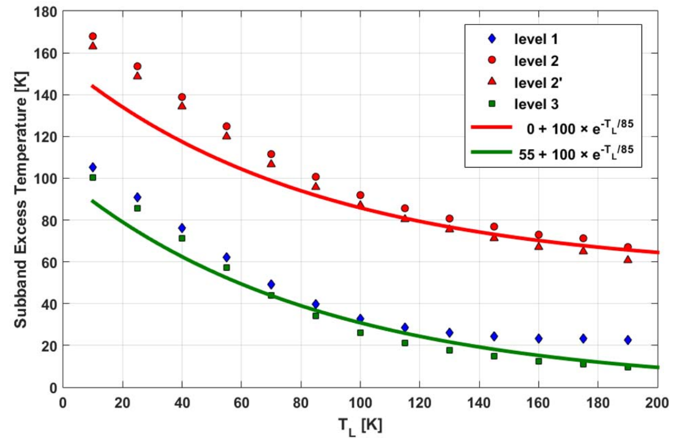

Fig. 3. Calculated subband excess temperatures (symbols) for a typical resonant phonon THz-QCL design [14], [25] as a function of lattice temperature. Solid lines represent the $T_{ex_{(3,2)}}(T_L)$ functions that are used in this work to describe the excess temperature of the upper (solid green line) and lower (solid red line) laser levels.

IV. Consequences for the Laser Performance

We use the electron transport schemes of Fig. 2 and the method outlined in [17] to reproduce P_{max} vs. temperature for the three devices investigated in this work. Calculation results for devices LB1, LB2 and HB are included in Fig. 1b, 1d and 1f, respectively, and we find very good agreement between calculated and experimental data in all cases. Used calculation parameters are summarized in Tab. II.

As in [17], we use for calculations a gain bandwidth of $\gamma_{32} = 1$ THz in all devices, which is a typical value for THz-QCLs [26], [27]. Very recently it has been reported that the gain bandwidth is increased in $GaAs/Al_{0.30}Ga_{0.70}As$ THz-QCLs with thin (<30 monolayers thick) wells due to the effect of interface roughness [28]. Device HB however uses relatively thick wells, so that we do not expect a larger value of γ_{32} in this device. We further use a total optical loss of $\alpha_{tot} = 12$ cm^{-1} for device LB1 and 16 cm^{-1} for devices LB2 and HB. The lower optical loss used for device LB1 is partially related to the less-lossy material (Cu) used in the metal-metal optical waveguide in device LB1 (devices LB2 and HB use Au-Au waveguides, which is expected to lead to somewhat larger optical loss values [29]). Additional sources of optical loss in devices LB2 and HB might arise from the increased doping in these samples [30]. Further calculation parameters are nominal design values as the calculated photon energy E_{32}, the doping level N_{tot}, the module length L_{mod}, intersubband energy spacing values E_{a3} and $E_{a_2} = E_{a_3} + h\nu$, raw electron-LO-phonon scattering times τ_{ij}^0, resonant tunneling times τ_{ij}^*, and total transmission coefficients T_3 and T_2. The only additional calculation parameters are the populations of upper and lower laser levels, N_3 and N_2, respectively, which are taken to $N_3 = 0.3N_{tot}$ and $N_2 = 0.06N_{tot}$ [17]. For further details on the calculation methodology we refer the interested reader to [17].

We observe from Fig. 1b, 1d and 1f that our calculation approach not only explains the measured T_{max} values, yet it also reproduces the P_{max} dependence on temperature over

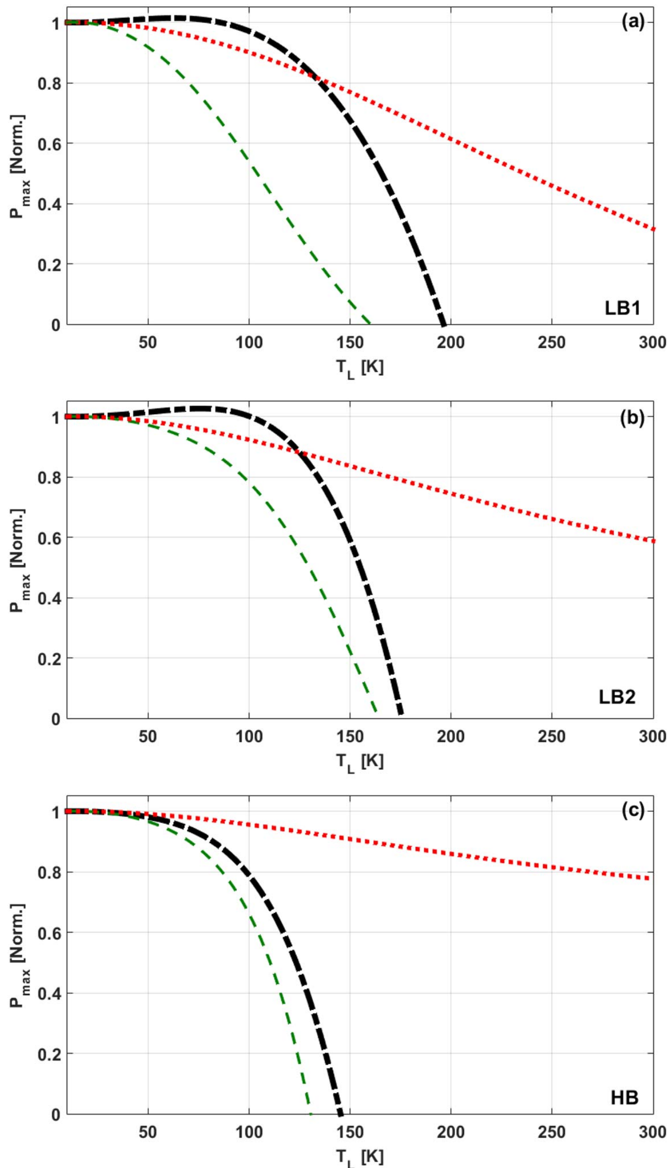

Fig. 4. Calculated light output power vs. temperature for device (a) LB1, (b) LB2 and (c) HB in three different scenarios. The dotted red line represents complete suppression of carrier escape from upper and lower laser levels, the dashed green line represents complete suppression of carrier escape from the lower laser level and the dashed-dotted black line includes all thermally activated non-radiative scattering paths. The dashed-dotted black line is the same curve as in Fig. 1b, 1d and 1f.

the entire device operation range. The latter is particularly important to understand the impact of the individual thermally activated leakage channels on the laser performance. To illustrate this we plot in Fig. 4 calculated P_{max} values under three different scenarios, which are (i) complete suppression of carrier escape from upper and lower laser levels (dotted red line), (ii) complete suppression of carrier escape from the LLL (dashed green line) and (iii) inclusion of all thermally activated non-radiative scattering paths (dashed-dotted black line). Scenario (iii) is the same curve as in Fig. 1b, 1d and 1f.

We see in Fig. 4 that exclusion of thermally activated escape paths leads to a nearly continuous decay of P_{max} as the temperature increases (dotted red line). In this case the decrease of P_{max} is driven by thermally activated scattering of electrons from the upper into the lower laser level via LO-phonon emission. As discussed in [14], the correspondent activation energy in this case is $E_{LO} - E_{32} \sim 20$ meV, i.e. the difference between LO-phonon and the photon energies. Device LB1 has a larger oscillator strength and suffers consequently of larger LO-phonon emission from the upper into the lower laser level. Consequently, calculated normalized P_{max} values in this scenario decay faster in device LB1 compared to devices LB2 and HB.

Addition of thermally activated escape of electrons out of the upper laser level leads to a sharper decay of P_{max} as the temperature increases (dashed green lines in Fig. 4). For the case of devices LB1 and LB2 (and in accordance to Fig. 3a) we consider thermally activated escape into the continuum through an excited resonant state (state 4 in device LB1 and state 5 in device LB2). From Tab. I we know that device LB1 has very large injector and extractor anticrossing energies ($\sim$2.8 meV and $\sim$5.9 meV, respectively), while device LB2 has moderate values ($\sim$1.6 meV and $\sim$3.7 meV, respectively). Since large anticrossing energies and large oscillator strengths require thinner barriers, it is reasonable that carrier escape in device LB1 will onset trough an energetically lower laying resonance. For the case of device HB (and in accordance to Fig. 3b) we consider thermally activated escape of electrons from the upper laser level into state 5 followed by tunneling through one (6.4 monolayers) barrier and relaxation to the lower laser level. This leakage path acts in parallel to standard electron LO-phonon emission, it degrades the temperature performance of the device and is absent in devices LB1 and LB2 (Fig. 2).

Comparison of dashed green lines and dashed-dotted black lines in Fig. 4 shows that thermally activated escape of electron out of the lower laser level leads to larger P_{max} values. As discussed in [17], this kind of leakage depopulates the lower laser level fast enough to effectively counteract the population inversion reduction that arises from the remaining leakage paths. As a consequence, nearly constant values of P_{max} are observed over a wide ($10 - 110$ K for LB1 and $10 - 120$ K for LB2) temperature range. In device HB this temperature-stabilization effect is virtually absent due to the strong reduction of this leakage mechanism as a consequence of the high $Al_{0.30}Ga_{0.70}As$ barriers. Altogether, in all devices, the output power drop as the temperature increases is delayed by the virtue of thermally activated carrier escape out of the lower laser level, ultimately leading to a larger values of T_{max} (200 K for LB1, 177 K for LB2 and 150 K for HB).

We further see in Fig. 4 that the effect of thermally activated leakage out of the lower laser level is especially pronounced in device LB1, increasing T_{max} from $\sim$155 K (dashed green line in Fig. 4a) to $\sim$200 K (dashed-dotted black in Fig. 4a). This is a direct consequence of the low activation energy together with the thinner barriers used in this design. In addition, the lower optical loss of device LB1 contributes to the strong temperature performance of this device.

A specific improvement direction on device LB1 would be to slow down thermally activated electron escape from

TABLE II
CALCULATION PARAMETERS

Device	E_{32} (meV)	N_{tot} (10^{10} cm^{-2})	α_{tot} (cm^{-1})	γ_{32} (THz)	L_{mod} (nm)	τ_{31}^0 (ps)	τ_{32}^0 (ps)	τ_{21}^0 (ps)	$\tau_{1'3}^*$ (ps)	$\tau_{2'2}^*$ (ps)	E_{a3} (meV)	E_{a2} (meV)	T_3	T_2
LB1	12	3	12	1	43.9	42	0.46	0.68	1.9	0.58	40	52	0.036	0.046
LB2	16	5.9	16	1	47.1	392	1.69	0.81	5.4	0.88	66	82	0.063	0.128
HB	17.3	5.9	16	1	47.1	190	1.61	0.43	3.7	0.63	58	75.3	0.109	0.027

Indicated are, from left to right, the device name, calculated photon energy, total sheet density per module, total optical loss, gain bandwidth, module length, τ_{31}^0 (raw scattering time for electron-LO phonon scattering between states 3 and 1), τ_{32}^0 (raw scattering time for electron-LO phonon scattering between states 3 and 2), τ_{21}^0 (effective scattering time from level $2'$ into level 1), τ_{ij}^* resonant tunneling time between states i and j, activation energies and total transmission coefficients. Note that electrons in level $2'$ can reach level 1 in two ways: they can either scatter directly into level 1 through LO-phonon emission or scatter first into level 2 by resonant tunneling and then relax into level 1 by LO-phonon emission. For further details on the calculation methodology we refer the interested reader to [17].

the upper laser level by inducing higher energetically-lying resonances and simultaneously conserving the fast electron escape path from the lower laser level.

V. CONCLUSION

To summarize, we analyzed light output power versus temperature profiles of state of the art terahertz quantum cascade lasers and identified specific thermally activated leakage paths responsible for the laser performance degradation as the temperature increases. We found that GaAs/$Al_{0.15}Ga_{0.85}As$ devices suffer from carriers escape into the continuum while this leakage path is strongly reduced in the GaAs/$Al_{0.30}Ga_{0.70}As$ device. Furthermore, although the usage of high barriers in the active region design eliminates carrier leakage from the upper laser level into the continuum, it also opens a non-radiative scattering path from the upper into the lower laser level parallel to standard LO-phonon emission. We also illustrated how leakage from the lower laser level into the continuum is enhanced in a GaAs/$Al_{0.15}Ga_{0.85}As$ device with thin barriers, significantly improving the laser performance (T_{max} = 200 K). These results clearly point out to a potential improvement direction in the design of highly temperature-insensitive THz-QCLs, namely to minimize thermally activated leakage from the upper laser level and maximize thermally activated leakage from the lower laser level. Using variable barriers in the active region design might be an effective implementation of this design strategy. Our approach represents a straightforward method to analyze and troubleshoot thermally-activated carrier leakage dynamics in THz-QCLs.

ACKNOWLEDGMENT

The authors gratefully acknowledge Prof. Qing Hu for his support in performing this research. The authors further thank John L. Reno for the MBE growths. A. Albo acknowledges the generosity and support of the Bar-Ilan University Engineering Faculty Fellowship as well as of the MIT-Technion and the Andrew and Erna Finci Viterbi Fellowships. Y. V. F. acknowledges the support of the Research Fellowship Program of the German Research Foundation, DFG (Grant FL945/1-1).

REFERENCES

[1] R. Köhler *et al.*, "Terahertz semiconductor-heterostructure laser," *Nature*, vol. 415, pp. 156–159, May 2002.
[2] J. R. Gao *et al.*, "Terahertz heterodyne receiver based on a quantum cascade laser and a superconducting bolometer," *Appl. Phys. Lett.*, vol. 86, no. 24, p. 244104, 2005.
[3] H.-W. Hübers *et al.*, "Terahertz quantum cascade laser as local oscillator in a heterodyne receiver," *Opt. Exp.*, vol. 13, no. 15, pp. 5890–5896, 2005.
[4] H. Richter *et al.*, "4.7-THz local oscillator for SOFIA based on a quantum-cascade laser," in *Proc. 39th Int. Conf. Infr., Millim., Terahertz Waves (IRMMW-THz)*, Tucson, AZ, USA, Sep. 2014, p. 1, doi: 10.1109/IRMMW-THz.2014.6956456.
[5] S. Fathololoumi *et al.*, "Terahertz quantum cascade lasers operating up to ~ 200 K with optimized oscillator strength and improved injection tunneling," *Opt. Exp.*, vol. 20, no. 4, pp. 3866–3876, 2012.
[6] M. S. Vitiello, G. Scalari, B. Williams, and P. De Natale, "Quantum cascade lasers: 20 years of challenges," *Opt. Exp.*, vol. 23, no. 4, pp. 5167–5182, 2015.
[7] C. Pflügl *et al.*, "Activation energy study of electron transport in high performance short wavelengths quantum cascade lasers," *Opt. Exp.*, vol. 18, no. 2, pp. 746–753, 2010.
[8] D. Botez, S. Kumar, J. C. Shin, L. J. Mawst, I. Vurgaftman, and J. R. Meyer, "Temperature dependence of the key electro-optical characteristics for midinfrared emitting quantum cascade lasers," *Appl. Phys. Lett.*, vol. 97, no. 7, p. 071101, 2010.
[9] D. Botez *et al.*, "The temperature dependence of key electro-optical characteristics for mid-infrared emitting quantum cascade lasers," *Proc. SPIE*, vol. 7953, p. 79530N, Feb. 2011.
[10] Y. V. Flores *et al.*, "Thermally activated leakage current in high-performance short-wavelength quantum cascade lasers," *J. Appl. Phys.*, vol. 113, no. 13, p. 134506, 2013.
[11] Y. V. Flores, G. Monastyrskyi, M. Elagin, M. P. Semtsiv, and W. T. Masselink, "Analysis of thermally activated leakage current in a low-threshold-current quantum-cascade laser emitting at 3.9 μm," *Proc. SPIE*, vol. 8640, p. 86401S, Mar. 2013.
[12] Y. V. Flores *et al.*, "Leakage current in quantum-cascade lasers through interface roughness scattering," *Appl. Phys. Lett.*, vol. 103, no. 16, p. 161102, 2013.
[13] D. Botez, C.-C. Chang, and L. J. Mawst, "Temperature sensitivity of the electro-optical characteristics for mid-infrared (λ= 3−16~μm)-emitting quantum cascade lasers," *J. Phys. D, Appl. Phys.*, vol. 49, no. 4, p. 43001, 2016.
[14] A. Albo and Q. Hu, "Investigating temperature degradation in THz quantum cascade lasers by examination of temperature dependence of output power," *Appl. Phys. Lett.*, vol. 106, no. 13, p. 131108, 2015.
[15] A. Albo and Q. Hu, "Carrier leakage into the continuum in diagonal GaAs/$Al_{0.15}$GaAs terahertz quantum cascade lasers," *Appl. Phys. Lett.*, vol. 107, no. 24, p. 241101, 2015.
[16] A. Albo, Q. Hu, and J. L. Reno, "Room temperature negative differential resistance in terahertz quantum cascade laser structures," *Appl. Phys. Lett.*, vol. 109, no. 8, p. 081102, 2016.

[17] A. Albo and Y. V. Flores, "Temperature-driven enhancement of the stimulated emission rate in terahertz quantum cascade lasers," *IEEE J. Quantum Electron.*, vol. 53, no. 1, Feb. 2017, Art. no. 2300105.

[18] B. S. Williams, S. Kumar, H. Callebaut, Q. Hu, and J. L. Reno, "Terahertz quantum-cascade laser at λ 100 μm using metal waveguide for mode confinement," *Appl. Phys. Lett.*, vol. 83, no. 11, p. 2124, 2003.

[19] C. W. I. Chan, A. Albo, Q. Hu, and J. L. Reno, "Tradeoffs between oscillator strength and lifetime in terahertz quantum cascade lasers," *Appl. Phys. Lett.*, vol. 109, no. 20, p. 201104, 2016.

[20] J. Faist, *Quantum Cascade Lasers*. Oxford, U.K.: Oxford Univ. Press, 2013.

[21] S. Kumar, C. W. I. Chan, Q. Hu, and J. L. Reno, "Two-well terahertz quantum-cascade laser with direct intrawell-phonon depopulation," *Appl. Phys. Lett.*, vol. 95, no. 14, p. 141110, 2009.

[22] P. Harrison and A. Valavanis, *Quantum Wells, Wires and Dots: Theoretical and Computational Physics of Semiconductor Nanostructures*, 4th ed. West Sussex, U.K.: Wiley, 2016.

[23] P. Harrison, D. Indjin, and R. W. Kelsall, "Electron temperature and mechanisms of hot carrier generation in quantum cascade lasers," *J. Appl. Phys.*, vol. 92, no. 11, p. 6921, 2002.

[24] V. Spagnolo, G. Scamarcio, H. Page, and C. Sirtori, "Simultaneous measurement of the electronic and lattice temperatures in $GaAs/Al_{0.45}Ga_{0.55}As$ quantum-cascade lasers: Influence on the optical performance," *Appl. Phys. Lett.*, vol. 84, no. 18, p. 3690, 2004.

[25] C. W. I. Chan, "Towards room-temperature terahertz quantum cascade lasers: Directions and design," Ph.D. dissertation, Dept. Elect. Eng. Comput. Sci., Massachusetts Inst. Technol., Cambridge, MA, USA, 2015.

[26] B. S. Williams, H. Callebaut, S. Kumar, Q. Hu, and J. L. Reno, "3.4-THz quantum cascade laser based on longitudinal-optical-phonon scattering for depopulation," *Appl. Phys. Lett.*, vol. 82, no. 7, p. 1015, 2003.

[27] D. Burghoff, T.-Y. Kao, D. Ban, A. W. M. Lee, Q. Hu, and J. Reno, "A terahertz pulse emitter monolithically integrated with a quantum cascade laser," *Appl. Phys. Lett.*, vol. 98, no. 6, p. 061112, 2011.

[28] Y. V. Flores and A. Albo, "Impact of interface roughness scattering on the performance of $GaAs/Al_xGa_{1-x}As$ terahertz quantum cascade lasers," *IEEE J. Quantum Electron.*, vol. 53, no. 3, Jun. 2017, Art. no. 2300208; and Erratum: Y. V. Flores and A. Albo, *IEEE J. Quantum Electron.*, vol. 53, no. 5, 2017.

[29] M. A. Belkin *et al.*, "Terahertz quantum cascade lasers with copper metal-metal waveguides operating up to 178 K," *Opt. Exp.*, vol. 16, no. 5, pp. 3242–3248, 2008.

[30] L. Ajili, G. Scalari, M. Giovannini, N. Hoyler, and J. Faist, "Doping in quantum cascade lasers. II. $GaAs/Al_{0.15}Ga_{0.85}$as terahertz devices," *Appl. Phys. Lett.*, vol. 100, no. 4, p. 043102, 2006.

Asaf Albo received the B.Sc. degrees (Hons.) in physics and materials engineering from the Technion, Israel Institute of the Technology, in 2002, the M.Sc. degree from the Department of Materials Engineering, Technion, Israel Institute of the Technology, in 2005, and the Ph.D. degree from the Department of Electrical Engineering, Technion, Israel Institute of the Technology, in 2011. He was a Research and Development Senior Physicist in the semiconductor industry for four years from 2010 to 2013. He was also a Research Fellow/Associate with the Research Laboratory of Electronics of the Massachusetts Institute of Technology for another four years from 2013 to 2017, where he was involved in the study of carrier dynamics in terahertz QCLs and developed novel design strategies for high-performance intersubband lasers for terahertz light emission. He joined the Faculty of Engineering, Bar-Ilan University, Israel. He is also a Materials and Devices Researcher that specializes in semiconductors, quantum-structures and their optoelectronic devices.

Yuri V. Flores was born in Baku, Azerbaijan, in 1986. He received the B.Sc. degree from the Leibniz University of Hannover, Hannover, Germany, in 2010, and the M.Sc. degree and the Ph.D. degree (Hons.) from Humboldt University Berlin, Germany, in 2013 and 2015, respectively, all in physics. He gained research experience at the Institute of Transport and Automation Technology, Hannover, where he was involved in developing software tools for RFID applications and at the Ferdinand-Braun-Institute, Berlin, where he was involved in conducting characterization studies on (Al,In,Ga)N ultraviolet LDs and LEDs. His research at Humboldt University focused on the development of high-power mid-infrared (Al,In,Ga)As quantum cascade lasers strain-balanced to InP, which led to the development of novel scientific approaches to investigate temperature-driven carrier leakage phenomena. He is currently a Post-Doctoral Research Fellow with the Research Laboratory of Electronics, Massachusetts Institute of Technology, where he is involved in studying the carrier dynamics in terahertz QCLs and developing novel design strategies for high-performance terahertz light-emitting semiconductor lasers.